JGR Space Physics

RESEARCH ARTICLE
10.1029/2020JA027802

The Polar Wind Modulated by the Spatial Inhomogeneity of the Strength of the Earth's Magnetic Field

Kun Li[1], Matthias Förster[2,3], Zhaojin Rong[4,5], Stein Haaland[2,6], Elena Kronberg[2,7], Jun Cui[1,8], Lihui Chai[4,5], and Yong Wei[4,5]

[1]Planetary Environmental and Astrobiological Research Laboratory (PEARL), School of Atmospheric Sciences, Sun Yat-sen University, Zhuhai, China, [2]Max Planck Institute for Solar System Research, Göttingen, Germany, [3]German Research Centre for Geosciences, Helmholtz Centre Potsdam, Potsdam, Germany, [4]Institute of Geology and Geophysics, Chinese Academy of Sciences, Beijing, China, [5]College of Earth and Planetary Sciences, University of Chinese Academy of Sciences, Beijing, China, [6]Birkeland Centre for Space Science, University of Bergen, Bergen, Norway, [7]Department of Earth and Environmental Sciences, Ludwig Maximilian University of Munich, Munich, Germany, [8]Chinese Academy of Sciences, Key Laboratory of Lunar and Deep Space Exploration, National Astronomical Observatories, Beijing, China

Key Points:
- The density and the particle flux of the polar wind are revealed to be anticorrelated with the strength of the Earth's magnetic field
- The polar rain can be the main energy source of the polar wind in the southern hemisphere during periods of high solar activity levels
- A strong magnetic field diminishes energy depositions in the polar cap and thus controls the density and particle flux of the polar wind

Correspondence to:
K. Li,
likun37@mail.sysu.edu.cn

Citation:
Li, K., Förster, M., Rong, Z., Haaland, S., Kronberg, E., Cui, J., et al. (2020). The Polar Wind Modulated by the Spatial Inhomogeneity of the Strength of the Earth's Magnetic Field. *Journal of Geophysical Research: Space Physics*, *125*, e2020JA027802. https://doi.org/10.1029/2020JA027802

Received 12 JAN 2020
Accepted 10 MAR 2020
Accepted article online 25 MAR 2020

Abstract When the geomagnetic field is weak, the small mirror force allows precipitating charged particles to deposit energy in the ionosphere. This leads to an increase in ionospheric outflow from the Earth's polar cap region, but such an effect has not been previously observed because the energies of the ions of the polar ionospheric outflow are too low, making it difficult to detect the low-energy ions with a positively charged spacecraft. In this study, we found an anticorrelation between ionospheric outflow and the strength of the Earth's magnetic field. Our results suggest that the electron precipitation through the polar rain can be a main energy source of the polar wind during periods of high levels of solar activity. The decreased magnetic field due to spatial inhomogeneity of the Earth's magnetic field and its effect on outflow can be used to study the outflow in history when the magnetic field was at similar levels.

Plain Language Summary Earth, Venus, and Mars have very different atmospheres although they are thought to possess similar atmospheres about 4.5 billion years ago. One of the main reasons considered for the losses of H_2O and O_2 is dramatic decreases in the dipole magnetic field on Venus and Mars. Although the Earth has kept its intrinsic magnetic field, there are variations in both orientation and strength. Previous observations have confirmed that atmospheric loss is controlled by the orientation of the geomagnetic dipole. However, the effect of variations in the strength of the Earth's magnetic field on atmospheric outflow has not been addressed. In this study, we have focused on the polar wind, the dominant ionospheric outflow from the polar regions. Our results reveal an anticorrelation between the outflow and the strength of the Earth's magnetic field, offering us a clue on the ionospheric and atmospheric evolution with a changing magnetic field.

1. Introduction

Over the last few decades, ionospheric outflow has been recognized as a significant supplier to the plasma in the Earth's magnetosphere (Chappell et al., 1987). Outflow plays an important role in magnetosphere-ionosphere coupling and magnetospheric dynamics. It is also believed that the ionospheric outflow could affect the evolution of the atmosphere (Moore & Horwitz, 2007; Wei et al., 2014; Yamauchi, 2019).

Among various ion escape mechanisms, the polar wind is attributed to a significant amount of ions escaping from the polar cap ionosphere (Axford, 1968; Banks & Holzer, 1968; Ganguli, 1996; Yau et al., 2007). At low altitudes, electrons have higher velocities than ions. The different scale heights between electrons and ions form an ambipolar electric field along the magnetic field lines. As the magnetic field lines in the polar caps are open and extended to the magnetotail lobes, ions primarily extracted by the ambipolar electric field could eventually escape and enter the magnetotail. Because of their ionospheric origin, ions in the polar wind are characterized as cold ions with both thermal energies and kinetic energies lower than a few tens of eV. Due to their low energies, cold ions of the polar wind are difficult to measure with an ion spectrometer on a positively charged spacecraft.

Both solar radiation and solar wind energy input are considered to drive the polar wind outflow. The solar radiation, containing extreme ultraviolet (EUV) radiation is essential for the formation of the ionosphere

and ions available for outflow (André et al., 2015; Engwall et al., 2009). Heating due to lower frequency radiation (e.g., in infrared ranges) enhances the ambipolar electric field and the polar wind outflow. The solar wind energy input, on the other hand, causes particle precipitation and Joule heating in the polar cap, for example, as calculated by Lu et al. (2016) for a geomagnetic storm. In the polar cap, the superthermal electrons in the solar wind precipitate along the open field lines in the magnetotail to the ionosphere with energies of a few hundreds of eV (Newell et al., 2009). Electron precipitation through this mechanism is defined as the polar rain, which could be one of the main energy sources of the polar wind. However, it is still not clear whether the polar rain influences the polar wind.

The polar wind is also influenced by the changes in the Earth's magnetic field. The diurnal and seasonal changes in the dipole tilt angle of the geomagnetic field have been found to influence the polar wind. The dipole tilt angle modulates the solar zenith angle (SZA) and hence the solar irradiation over the polar cap around the dipole axis. This effect has been addressed in both simulations (e.g., Barakat et al., 2015; Glocer et al., 2012; Su et al., 1998) and observations (e.g., Kitamura et al., 2011; Li et al., 2017, 2018; Maes et al., 2017). Furthermore, the dipole tilt angle also influences magnetosphere-ionosphere coupling as simulated by Cnossen and Richmond (2012). In addition, the review paper of Laundal et al. (2017) gives a comprehensive survey of the north-south asymmetries in the magnetic field at polar latitudes and their consequences for magnetosphere-ionosphere-thermosphere coupling.

The strength of the Earth's magnetic field is thought to affect the ionospheric outflow. With a strong magnetic field in the polar cap, a large upward magnetic mirror force allows the precipitating plasma with constant energy to penetrate shallow into the ionosphere. As the polar rain is relatively homogenous in the polar cap, there should be an anticorrelation between the polar wind and the strength of the Earth's magnetic field. However, this effect on the polar wind has not been addressed because of the difficulty in measuring the cold ions as mentioned above.

In this study, we have utilized a data set of cold ions to investigate the correlation relationship between the ion outflow (including density and particle flux) and the strength of the Earth's magnetic field.

2. Data and Methods

2.1. Cold Ion Outflow in the Topside Ionosphere

The method to derive the bulk velocity of cold ions in the magnetosphere has been introduced by Engwall et al. (2009). They have analyzed the wake electric field downstream of the Cluster spacecraft in flows of cold ions. With this method, André et al. (2015) have utilized measurements from two Cluster spacecraft (C1 and C3) from July to November during each year from 2001 to 2009 (C1) and 2010 (C3, excluding 2006), covering a large part of solar cycle 23. The number of records is approximately 330,000, and of these, approximately 320,000 records are identified as tailward flow.

The density of cold ions is derived from a functional dependence between spacecraft potential and ambient electron density (Lybekk et al., 2012), assuming the electric neutrality of plasma. It should be noted that the cold ion data set mainly contains information on protons because the wake method is more sensitive to light ions. Nevertheless, H^+ is the dominant population in the polar wind (Su et al., 1998). For details on data selection and error estimation, we refer to a previous study (André et al., 2015). Their data set contains the density (n_{mag}) and parallel velocity ($V_{||,\ mag}$) of cold ions in the magnetosphere.

To obtain the parallel velocity of cold ions in the topside ionosphere ($V_{||}$), Li et al. (2017) have conducted particle tracing with input from the above data set. In the particle tracing, the cold ions of the polar wind are considered to move in a magnetic flux tube, while the magnetic flux tube is moving tailward due to the magnetospheric convection. Along the magnetic field lines, cold ions experience accelerations such as those due to the centrifugal force and gravity. The motion of cold ions follows the guiding center equation. The magnetic field used for particle tracing is given by the Tsyganenko T01 model (Tsyganenko, 2002a, 2002b). Assuming the conservation of particle flux in a magnetic flux tube, the density of cold ions in the topside ionosphere (n) is obtained by $n = \frac{B^*\left(n_{mag}{}^*V_{\parallel,mag}\right)}{B_{mag}{}^*V_{\parallel}}$, where B and B_{mag} denote the strengths of the magnetic field in the ionosphere and the magnetosphere, respectively. Li et al. (2017) have found approximately 237,000

records of cold ion density, velocity, and particle flux ($F_P = nV_{||}$) at 1,000 km altitude. Their tracing results have been used in the study by Li et al. (2018) and in this study.

2.2. Sorting Data According to Internal Driver

The internal driver is the strength of the Earth's magnetic field ($|B|$ in the following). In the polar cap, the precipitation of charged particles is impeded by the local magnetic field close to the Earth. On one end of the field line in the magnetotail lobes where electrons start to precipitate toward the Earth, the strength of local magnetic field is measured as about 10 nT from approximately 30 to 220 Re (Slavin et al., 1985), although the field lines eventually connect to the Sun. On the other end of the field line at the surface of the Earth, $|B|$ varies from ~3×10^4 to ~6×10^4 nT due to spatial inhomogeneity of the Earth's magnetic field in the polar region. This leads to different gradients of the magnetic field strength along the field lines and hence different mirror forces for precipitating electrons from the magnetotail along the field lines with the same magnetic moment. A smaller $|B|$ at the surface of the Earth and thus a smaller overall magnetic mirror force allows an electron to penetrate deeper in the atmosphere/ionosphere, and to cause more heating and ionization. The heating due to collisions enhances the ambipolar electric field that accelerates ion outflow. The ionization provides oxygen ions for the charge exchange between oxygen ions and hydrogen atoms (Barakat et al., 1987; Richards & Torr, 1985). Therefore, the high density and flux of the proton-dominated polar wind tends to be observed at locations with small $|B|$. In this study, $|B|$ is obtained from the international geomagnetic reference field (IGRF11) model combined with the Tsyganenko T01 model.

For a long time, the southern hemisphere has been known to have a large inhomogeneity of $|B|$ in the polar cap at a fixed height compared to the northern hemisphere. The much larger range between minimum and maximum values of $|B|$ at a fixed height inside the polar cap, for example, in Figure 1 of Förster and Cnossen (2013), makes the southern hemisphere more favorable for this study. Therefore, we have only focused on the polar wind in the southern hemisphere.

2.3. Data Selection According to External Drivers

One of the external drivers of the polar wind is the solar wind energy in terms of Poynting flux that enters the polar cap ionosphere, which affects the Joule heating and particle precipitation. Both of these could be enhanced during times of enhanced geomagnetic activities. Several indices have been introduced to estimate the energies from the two mechanisms. For example, investigations on Joule heating as a function of the auroral electrojet (*AE*) index have been carried out by Ahn and Akasofu (1983) and Baumjohann and Kamide (1984). Chun et al. (2002) have studied the correlation between Joule heating and the polar cap (PC) index. The *AE* index has also been found to correlate with the energy dissipation due to electron precipitation (Østgaard et al., 2002). In this study, we have used the *AE* index as an indicator of energy dissipation in the polar region from the two mechanisms.

Electron precipitation from the solar wind to the polar cap ionosphere via the open field lines in the magnetotail lobes, which is defined as the polar rain, depends on the sign of the x component of the interplanetary magnetic field (IMF) (Gosling et al., 1985; Newell et al., 2009). This is explained by field lines connecting to the solar wind. When the IMF B_x switches from negative to positive, the southern hemisphere becomes a favored hemisphere for the polar rain. The density of the precipitating electron is three to eight times higher in the favored hemisphere than that in the other hemisphere (Gosling et al., 1985), although the polar rain density does not correlate with the density of the solar wind (Riehl & Hardy, 1986). In the polar rain of either hemisphere, the halo and the core components of the solar wind electrons with low energies and isotropic distributions are commonly observed. Additionally, the field-aligned Strahl component of the solar wind electrons with relatively high energies is also commonly observed in the favored hemisphere (Fairfield & Scudder, 1985).

We have confined our selection of the data with IMF $B_x < 0$ for the southern hemisphere in the following statistics. Because the field lines in the favored hemisphere are more directly connected to the solar wind on the dayside than the nightside, the particle flux of electron precipitation exhibits a strong noon-midnight gradient (Gussenhoven & Madden, 1990), which affects the polar wind. In addition, the precipitating electrons have more field-aligned electrons in the hemisphere favored for the polar rain. They are more likely to be lost in the atmosphere. In terms of energizing the polar wind, they behave differently from the polar rain electrons

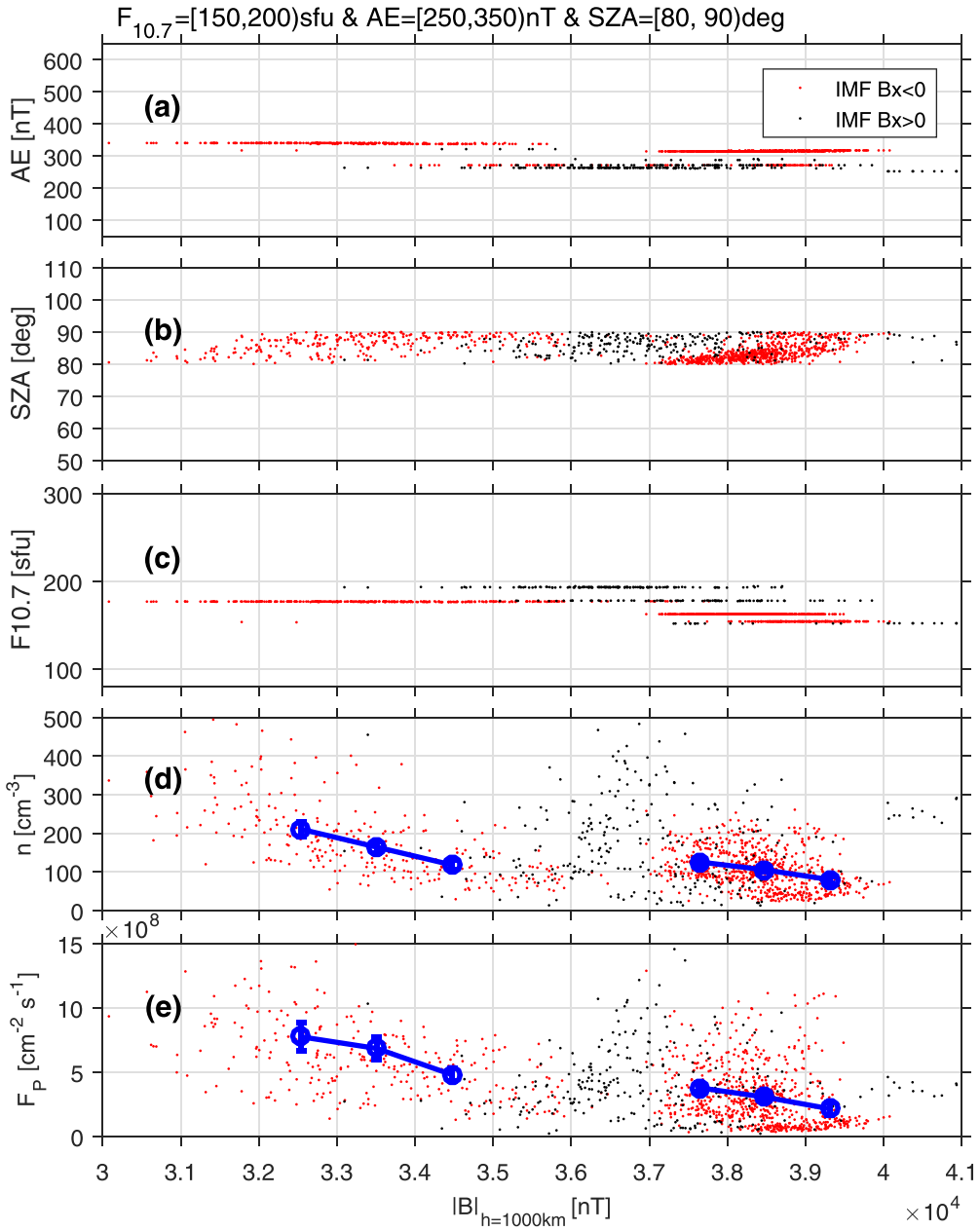

Figure 1. An example of identifying the anticorrelation between outflow and $|B|$ for outflow with the *AE* index between 250 and 350 nT and SZA between 80° and 90°, when the $F_{10.7}$ index was between 150 and 200 sfu. (ae) The *AE* index, SZA, the $F_{10.7}$ index, n, and F_P as functions of $|B|$ are shown, respectively. Where n and F_p are the density and the particle flux of cold ion outflow at the topside ionosphere, respectively. The red and black dots represent the values for IMF $B_x < 0$ and for IMF $B_x > 0$, respectively. The blue circles and vertical bars in Figures 1d and 1e represent the 99% confidence intervals and the mean values, respectively, for IMF $B_x < 0$ in each interval of $|B|$ (10^3 nT cadence). The confidence intervals and mean values are calculated for the intervals with more than 40 data points. Some of the confidence intervals overlap the mean values as they are sufficiently small compared to the scale of the *y*-axis.

in the unfavored hemisphere. The outflow densities and fluxes with IMF $B_x > 0$ are often larger than those with IMF $B_x < 0$. This is demonstrated in Figures 1d and 1e as an example and is explained in section 3.

Another external driver is the solar EUV irradiation which can be parameterized by the $F_{10.7}$ index. To eliminate the effect of a large variation in the $F_{10.7}$ index during the solar cycle, we have confined the data selection with respect to the $F_{10.7}$ index in a relatively narrow range (between 150 and 200 sfu). Outflow in other ranges will also be discussed at the end of the next section.

With the Earth's rotation and revolution, the diurnal and seasonal changes in the dipole tilt angle modify the SZA within the polar cap surrounding the dipole axis, which eventually modulates the EUV irradiation over the polar cap. As there is only a small variation in the $F_{10.7}$ index of selected data, we have used the SZA to sort the data.

3. Observational Results

Figure 1 shows an example in which all the records have been collected when the *AE* index was between 250 and 350 nT, SZA was between 80° and 90°, and the $F_{10.7}$ index was between 150 and 200 sfu. With these criteria, approximately 1,300 data points recorded in 8 days have been selected. Of these, approximately 980 data points have been found with IMF $B_x < 0$. From top to bottom, Figure 1 shows the *AE* index, SZA, the $F_{10.7}$ index, n, and F_P as functions of $|B|$, respectively. The red dots in each panel represent the parameters for outflows with IMF $B_x < 0$. For IMF $B_x < 0$, the blue vertical bars and circles in Figures 1d and 1e represent the 99% confidence intervals and the mean values of the corresponding outflow parameters in each 10^3 nT interval of $|B|$, respectively. Values calculated from less than 40 data points in each 10^3 nT interval of $|B|$ are removed for reliability, although requiring at least 30 or 50 data points does not change our conclusions. Figure 1d shows that the mean n decreases with increasing $|B|$, while all other parameters shown in Figures 1a1c do not systematically vary with $|B|$. Similarly, Figure 1e shows that the mean F_P is anticorrelated with $|B|$. The 99% confidence intervals are smaller than the variation of either n or F_P, indicating that uncertainties of measurement are small compared to the variation of the outflow.

The black dots in Figure 1 represent the data selected with the same criteria on the $F_{10.7}$ index, the *AE* index, and SZA as those shown in red, except the IMF B_x being positive. When IMF B_x is positive, the southern hemisphere is favored for the polar rain, a larger density of the polar rain enables a higher density and particle flux of the polar wind than when the hemisphere is unfavored for the polar rain (shown in Figures 1d and 1e, respectively).

The data with $|B|$ at 1,000 km altitude being between 3.6×10^5 and 3.8×10^5 nT are used to quantify the effect of the polar rain, because the number of data points for IMF $B_x < 0$ is comparable to that for IMF $B_x > 0$. With fixed energy sources except the polar rain, our calculation shows that the mean value of n increased by approximately 50% as the hemisphere turns from unfavored to favored for the polar rain. Likewise, the polar rain causes an increase of approximately 20% in F_p. These increases are smaller than and comparable to that caused by the solar wind energy input in terms of Poynting flux and solar EUV, which are shown in Figure 3a (for n) and Figure 3c (for F_p) of Li et al. (2017).

A similar dependence of the outflow on the direction of IMF B_x is found in others ranges with the same and higher $F_{10.7}$, suggesting that the polar rain could be one of the main energy sources of the polar wind.

The anticorrelations between the outflow and $|B|$ were also identified in other subsets in various ranges of the *AE* index and SZA, with IMF $B_x < 0$, and $F_{10.7}$ index between 150 and 200 sfu. Following the same procedure as that in Figure 1, Figures 2 shows the mean values and the 99% confidence interval of n as a function of $|B|$ at 1,000 km altitude. Figure 3 shows the same as Figure 2, but for that of F_p. The anticorrelation is identified by the fact that the mean values of n or F_p decrease with increasing $|B|$, while there is no systematic change in other parameters. The confidence interval as a measure of uncertainty of measurement being smaller than variation is another criterion for identifying the anticorrelation. The ranges of the *AE* index and SZA for each subset are indicated in the corresponding panel. Only the subsets with sufficient data points and relatively large spans in $|B|$ (at least three mean values in the range of $|B|$ shown in each panel) for analysis are shown in these figures.

We have sorted these subsets into three categories. Category 1 is for the subsets in which both n and F_P are anticorrelated with $|B|$. In category 2 subsets, only n is anticorrelated with $|B|$. Category 3 denotes the subsets in which neither n nor F_p is anticorrelated with $|B|$. The category of each subset is indicated in the corresponding panel by the red-colored number.

Figure 4b shows an overview of identifying the anticorrelations in subsets with various ranges of *AE* index and SZA for the southern hemisphere when the $F_{10.7}$ index was between 150 and 200 sfu and

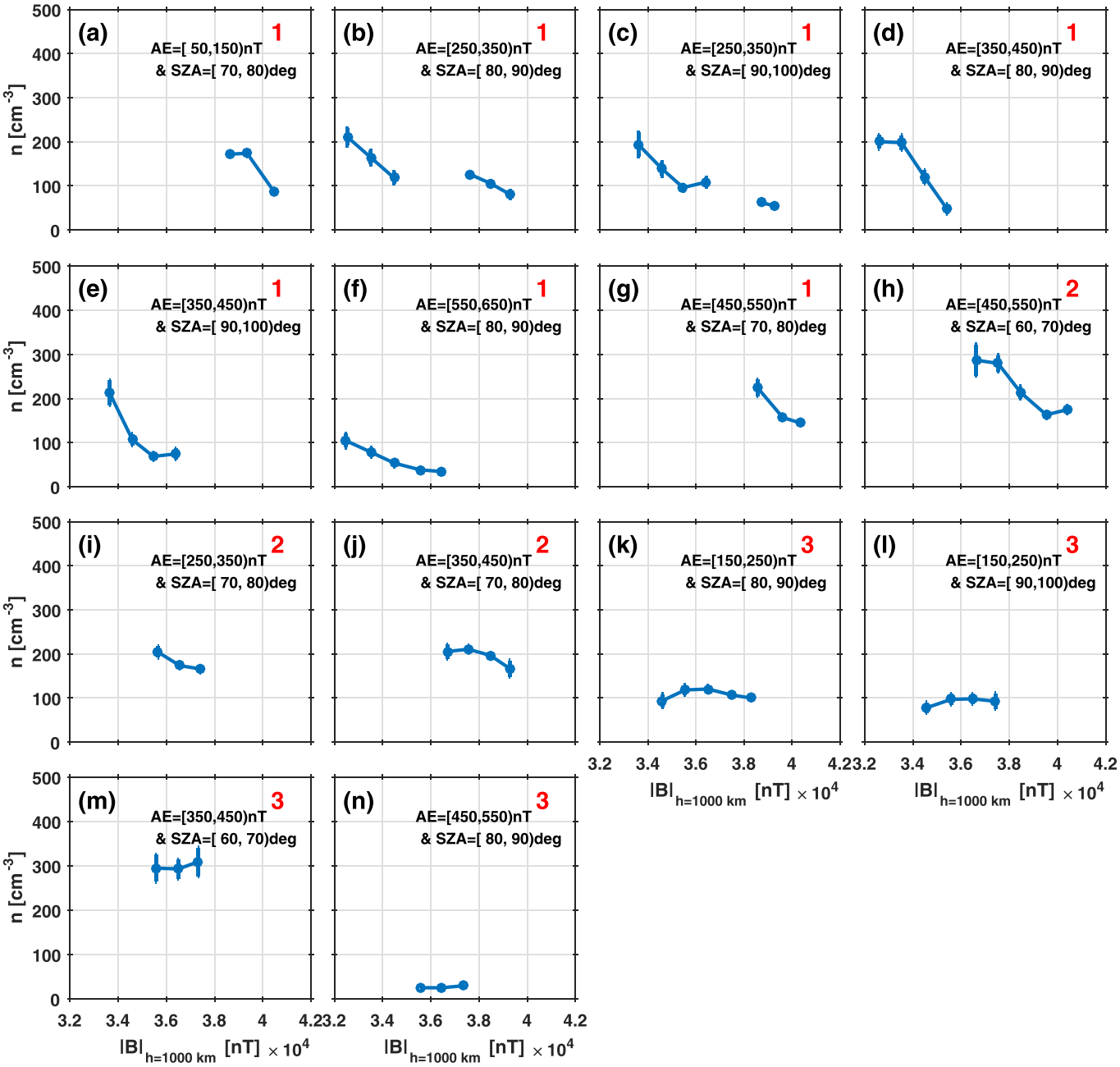

Figure 2. Mean values and 99% confidence intervals of n as functions of $|B|$ at 1,000 km altitude in various ranges of the AE index and SZA (indicated in each panel) when the $F_{10.7}$ index was between 150 and 200 sfu and IMF B_x was negative. All the subsets with sufficient numbers of data points and span in $|B|$ are included in this figure. The red-colored number in each panel indicates the category of the subset that is determined from the type of correlation between n, F_p, and $|B|$ as described in the text.

IMF B_x was negative. In total, approximately 23,000 records of polar wind were selected. The colored pixels indicate the numbers of data points. Numbers 1 and 2 in pixels denote categories 1 and 2 subsets of anticorrelation, respectively (they are also detailed in Figures 2 and 3). In addition to subsets of categories 1 and 2 anticorrelations, there are category 3 subsets in which the anticorrelation is not identified. The category 4 subsets are defined as the subsets in which the correlation cannot be identified because of a small number of data points or a small span in $|B|$. Here, the occurrence rate of the anticorrelation between n and $|B|$ is approximately 71% and was calculated from the number of

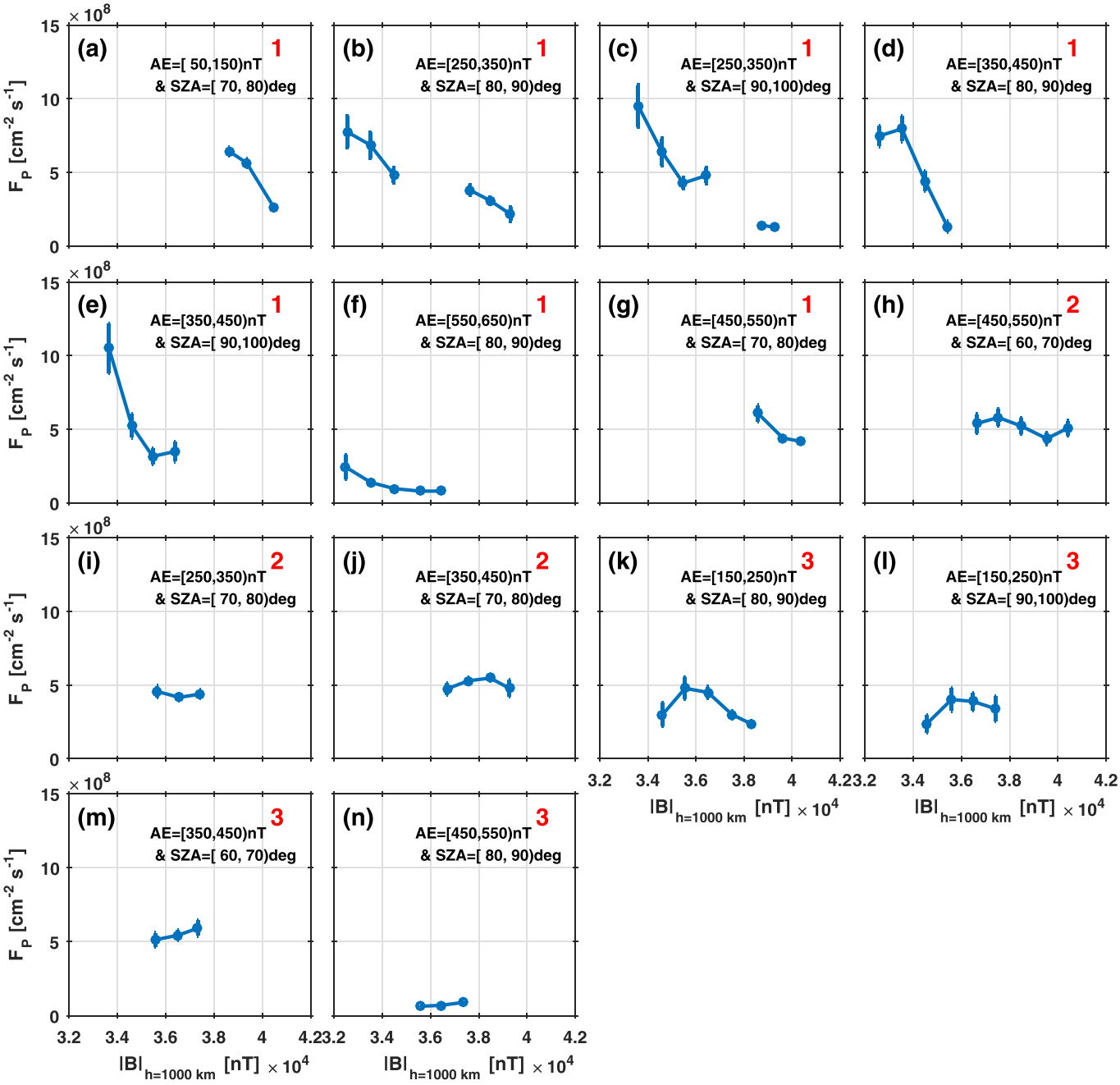

Figure 3. The same as Figure 2, but for the values of Fp. Compared to Figure 2, the anticorrelation does not appear in Figures 3h and 3i, suggesting they are the category 2 subsets. The subsets shown in Figures 3k3n are category 3 subsets, as the anticorrelation appears neither in Figures 2k2n nor in Figures 3k3n.

categories 1 and 2 subsets divided by the number of categories 1, 2, and 3 subsets. Similarly, the occurrence rate of the anticorrelation between F_P and $|B|$ is approximately 50%.

The same analysis procedure has been done for outflow with the $F_{10.7}$ index smaller than 150 sfu (approximately 20,000 data points). As demonstrated in Figure 4a, 17 subsets are found with sufficient data points and coverage in $|B|$. Two of them are identified as category 1 subsets in our data set. Figure 4c shows the analysis for the outflows with the $F_{10.7}$ index larger than 200 sfu (approximately 7,800 data points), only two out of eight subsets that contain sufficient data points with sufficient span in $|B|$ are identified with the anticorrelations. These results are summarized in Table 1.

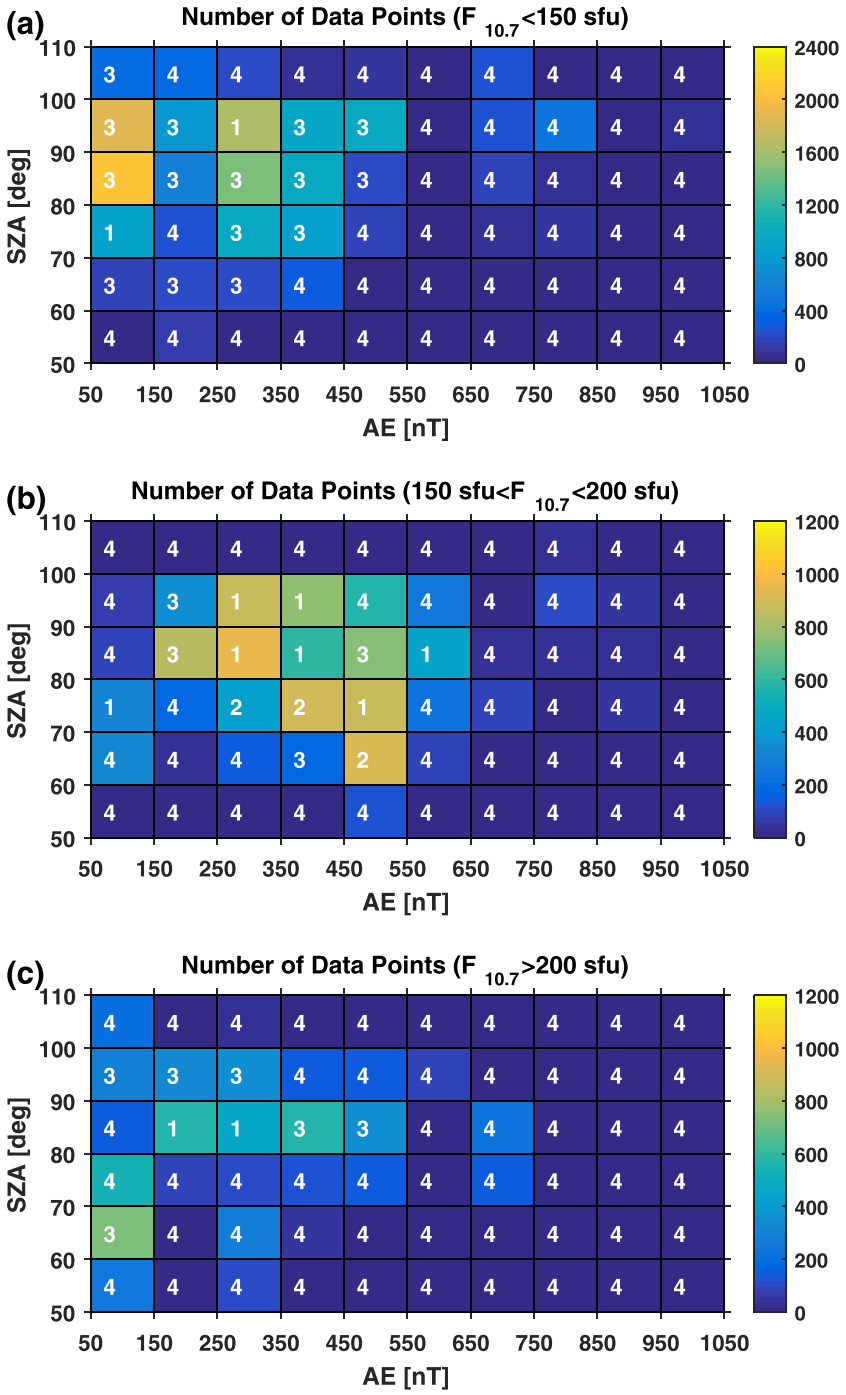

Figure 4. Results of analyzing anticorrelation between the polar wind and |*B*| in various ranges of the *AE* index and SZA with the $F_{10.7}$ index when IMF B_x was negative and the $F_{10.7}$ index was (a) below 150 sfu, (b) between 150 and 200 sfu, and (c) above 200 sfu. Pixels are color-coded by the numbers of data points in various ranges. The number in each panel indicates the result of analyzing anticorrelations as described in the text.

4. Discussion

Table 1 shows that the occurrence rate of the anticorrelations derived from our data set was the highest when the $F_{10.7}$ index was between 150 and 200 sfu. Our analysis shows that the occurrence rates are 12% and 25% when the $F_{10.7}$ index was lower than 150 sfu and higher than 200 sfu, respectively.

Table 1
Occurrence Rates of Anticorrelation and Numbers of Data Points for Different Levels of Solar Activity

Solar activity levels	Occurrence rates of the anticorrelations: Between n and $\|B\|$	Occurrence rates of the anticorrelations: Between F_p and $\|B\|$	Total number of data points
$F_{10.7}$ < 150 sfu	12% (2/17)	12% (2/17)	~20,000
150 sfu < $F_{10.7}$ < 200 sfu	71% (10/14)	50% (7/14)	~23,000
$F_{10.7}$ > 200 sfu	25% (2/8)	25% (2/8)	~7,800

The observed dependence of anticorrelation on solar activity can be explained as shown by the schematic sketch in Figure 5. During the periods of low solar activity with lower thermospheric temperatures and hence a contracted atmospheric layer (as shown in Figure 5a), the electrons from the polar rain may have a lower probability of access the atmosphere, that is, the topside ionosphere may be lower than the mirroring altitude of precipitating electrons. Under this condition, the ionospheric outflow is less likely correlated with $|B|$. During the high levels of solar activity, the topside atmosphere (thermosphere) expands to high altitudes. The atmosphere becomes accessible for the precipitating electrons, which are mirrored at different altitudes in the atmosphere depending on $|B|$. Therefore, there are anticorrelations between the outflow and $|B|$ as we have observed. Figure 5c shows that the topside atmosphere expands to even higher altitudes during periods of extremely high levels of solar activity. No matter how much mirror force they encounter, a large portion of the precipitating electrons collide with many particles and deposit all their energies. These electrons are eventually lost in the atmosphere. Only a few electrons are mirrored back to high altitudes. Therefore, a low occurrence rate of anticorrelation under this condition is expected.

For the $F_{10.7}$ index between 150 and 200 sfu, the disappearing of the anticorrelation in category 3 subsets may be attributed to occasional changes in the pitch angle distribution of the polar rain electrons, depending on the condition of the bow shock (Goodrich & Scudder, 1984). When the distributions of precipitating electrons with initial pitch angles close to 180° (Earthward in the southern hemisphere) are populated, they access the atmosphere and enhance the outflow, diminishing the anticorrelation between the outflow and $|B|$ that is caused by electrons with initial pitch angles smaller than 180° and eventually mirrored back to high altitudes. It is also possible that the precipitating electron population is dominated by electrons with initial pitch angles much smaller than 180°. This pitch angle distribution can be also attributed to the electric potential across the bow shock (Goodrich & Scudder, 1984). These electrons are mirrored by the magnetic field before entering the atmosphere, making the anticorrelation no longer obvious.

The fact that $|B|$ is on average smaller in the northern hemisphere than in the southern hemisphere may lead to larger energy deposition in the northern hemisphere, under similar conditions for the electron precipitation. This may be the cause of a higher density of cold ions in the northern lobe as observed by Haaland et al. (2017).

For a better understanding of the complex processes, one should carry out a simulation to reproduce the effects of the spatial inhomogeneity of the Earth's magnetic field on the polar wind outflow for various levels of solar activity. Considering invariance of the magnetic moment, the magnetic strength at the mirror altitude (B_{mirror}) can be calculated as $B_{mirror} = B_{lobe}/sin^2\alpha_{initial}$, where $\alpha_{initial}$ and B_{lobe} represent the initial pitch angle of electrons and the strength of local magnetic field in the lobe where electrons start to precipitate, respectively. The magnetic mirror altitude (H_{mirror}) is obtained from the magnetic models (the IGRF model combined with the Tsyganenko T01 model) with the input of B_{mirror}. As $|B|$ at the Earth's surface decreases from 6.7×10^4 to 5.5×10^4 nT in the southern polar cap region, our results indicate that H_{mirror} decreases from 408 to 51 km for $\alpha_{initial} = 179.2°$ and that H_{mirror} decreases from 1,039 to 555 km for $\alpha_{initial} = 179.1°$. In Figure 6, the ranges of the magnetic mirror altitudes for the precipitating electrons are marked by the blue areas. Using the NRLMSISE00 model (Picone et al., 2002), we have obtained the density profiles of the most dominant ionizable species (O and O_2).

Within the ranges of the magnetic mirror altitude, there are significant variations in the density of the atmosphere and thus in the efficiency of energy deposition. Figure 6a indicates that density of O at the lowest magnetic mirror altitude (for either $\alpha_{initial} = 179.1°$ or $\alpha_{initial} = 179.2°$) is about two to three orders of magnitude larger than that at the highest magnetic mirror altitude. The enhancement in the density of O_2 with decreasing altitude is even larger. This implies that the energy deposition due to particle collision at places with small $|B|$ could be greatly more efficient than that with large $|B|$.

We have also estimated the expansion of the thermosphere as a function of the $F_{10.7}$ index. For a given mirror altitude of precipitating electrons with $\alpha_{initial} = 179.1°$, for example, Figure 6b shows that the number density of O when $F_{10.7} = 160$ sfu is about 10 times that when $F_{10.7} = 90$ sfu. The number density of O

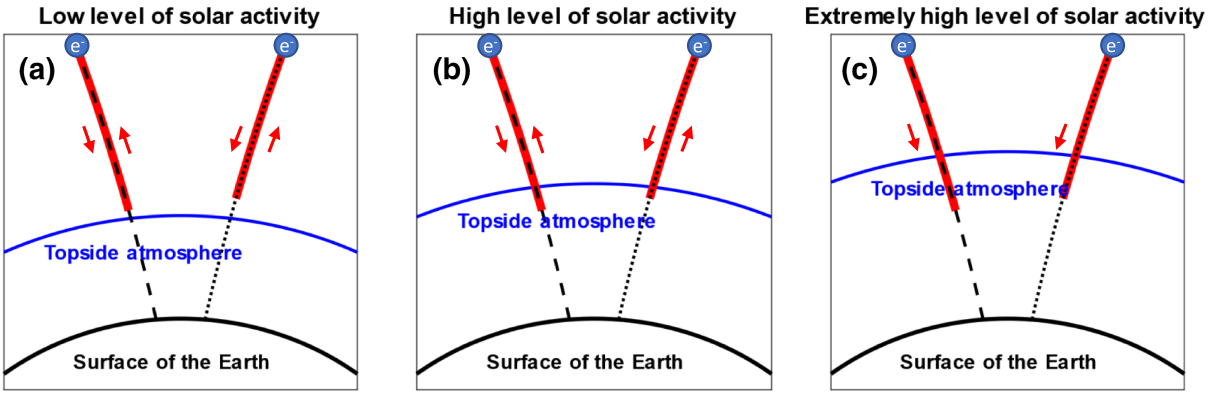

Figure 5. Schematic diagram showing the cause of dependence of the anticorrelation on solar activity. Dashed and dotted curves represent the magnetic field lines with the smallest and the biggest $|B|$, respectively. The trajectories of the guiding center of precipitating electrons are represented as the red solid curves. The red arrows indicate the directions of the downward moving electrons and the upward one if the electrons are mirrored. From left to right, each panel shows the situations with solar activity from low to high.

when $F_{10.7}$ = 250 sfu is about two orders of magnitude larger than that when $F_{10.7}$ = 90 sfu. The enhancement in the density of O_2 with increasing solar activity is even larger at high altitudes. These results imply that the energy deposition due to particle collision at times of extremely high solar activity could be greatly more efficient than that at times of low solar activity.

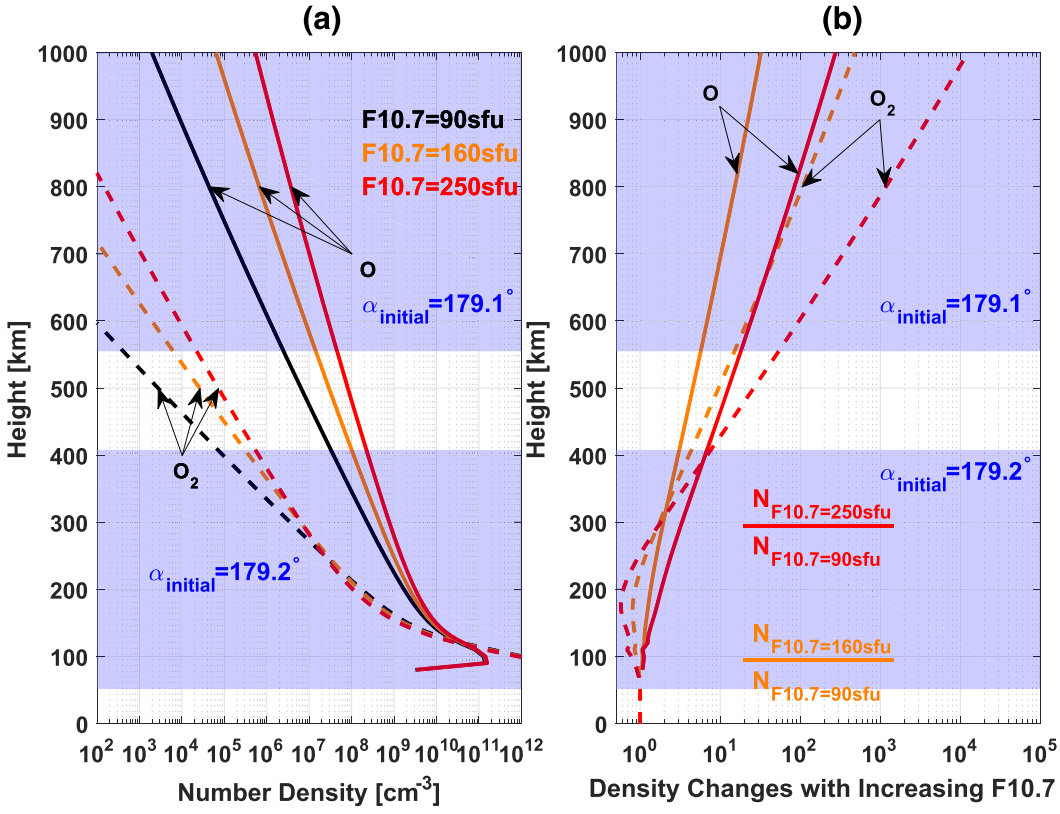

Figure 6. (a) Number density of O (solid curves) and O_2 (dashed curves) in the polar region as a function of altitude for three different $F_{10.7}$ indices that are obtained from the NRLMSISE00 model. The blue areas, as well as that in Figure 6b, indicate the ranges of the magnetic mirror altitudes for the precipitating electrons with initial pitch angles $\alpha_{initial}$ = 179.1° and $\alpha_{initial}$ = 179.2°. (b) Number density changes with increasing $F_{10.7}$ index as a function of altitude. The density changes at an altitude due to the increase in the $F_{10.7}$ index from 90 to 160 sfu (or from 90 to 250 sfu) are calculated as the density when $F_{10.7}$ = 160 (or $F_{10.7}$ = 250) divided by that when $F_{10.7}$ = 90.

The simulation should include the magnetic mirror force, charge exchange, and energy loss due to collisions (Green & Stolaski, 1976; Slinker et al., 1988), with considering of the pitch angle scattering of precipitating electrons in the upper atmosphere (e.g., Prasad et al., 1985), and the effects of secondary electrons produced by precipitating electrons (e.g., Varney et al., 2014). As an observational study, however, a more realistic simulation is beyond the scope of the present paper and will be focused in a later paper.

5. Conclusions

We have utilized the data set of cold ions with energies lower than a few tens of eV to study the correlation between the strength of the Earth's magnetic field and the polar wind. The main results of this study are the following:

1. Under the conditions where the $F_{10.7}$ index is between 150 and 200 sfu, the occurrence rate of the anticorrelation between density of the polar wind ion outflow and the strength of the Earth's magnetic field ($|B|$) in the southern hemisphere is approximately 71%. Meanwhile, the occurrence rate of the anticorrelation between the particle flux of the polar wind and $|B|$ is approximately 50%. The occurrence rate of the anticorrelation in other ranges of the $F_{10.7}$ index is much less because the atmosphere is not accessible for electrons in the polar rain when the $F_{10.7}$ index is extremely low, or the energy deposition by electron precipitation is not influenced by magnetic field strength when the $F_{10.7}$ index is extremely high.
2. The observed anticorrelation can be explained by the fact that the precipitating electrons along field lines with large $|B|$ deposit less energy in the ionosphere than those with small $|B|$. A strong magnetic field provides a large gradient of magnetic field along the field line and thus large magnetic mirror forces for precipitating electrons, which mirror electrons back to their initial altitude before depositing a fraction of their energies in the atmosphere.
3. The electron precipitation from the polar rain is one of the main energy sources for the polar wind. This is confirmed by our observation in the southern hemisphere during the period of high solar activity levels ($F_{10.7} > 150$ sfu). Our observation shows relatively large densities and particle fluxes of the polar wind when the southern hemisphere was favored for the polar rain. This mechanism may contribute to the north-south asymmetry in ionospheric outflow because the northern hemisphere has on average a smaller $|B|$ at ionospheric heights and a smaller spatial inhomogeneity in the magnetic field than the southern hemisphere.

Acknowledgments
This work is supported by the National Natural Scientific Foundation of China under Grants 41704164 and 41774188. Research efforts by SH are supported by the Norwegian Research Council under grant 223252. Work of EK is supported by German Science Foundation (DFG) under number KR 4375/2-1 within SPP 'Dynamic Earth'. The cold ion data set is based on the Cluster measurements available from the Cluster Science Archive (https://cosmos.esa.int/web/csa). Data selection, qualifying, and additional details are described by André et al. (20152015). The OMNI data for solar wind parameters are available online (https://omniweb.gsfc.nasa.gov/form/omni_min.html).

References

Ahn, B.-H. J., Akasofu, S.-I., & Kamide, Y. (1983). The Joule heat production rate and particle energy injection rate as a function of the geomagnetic indices AE and AL. *Journal of Geophysical Research*, *88*(6275–6287), 1983.

André, M., Li, K., & Eriksson, A. I. (2015). Outflow of low-energy ions and the solar cycle. *Journal of Geophysical Research: Space Physics*, *120*, 1072–1085. https://doi.org/10.1002/2014JA020714

Axford, W. I. (1968). The polar wind and the terrestrial helium budget. *Journal of Geophysical Research*, *73*, 6855–6859. https://doi.org/10.1029/JA073i021p06855

Banks, P. M., & Holzer, T. E. (1968). The polar wind. *Journal of Geophysical Research*, *73*,21 6846–6854. https://doi.org/10.1029/JA073i021p06846

Barakat, A. R., Eccles, J. V., & Schunk, R. W. (2015). Effects of geographic-geomagnetic pole offset on ionospheric outflow: Can the ionosphere wag the magnetospheric tail? *Geophysical Research Letters*, *42*, 8288–8293. https://doi.org/10.1002/2015GL065736

Barakat, A. R., Schunk, R. W., Moore, T. E., & Waite, J. H. Jr. (1987). Ion escape fluxes from the terrestrial high-latitude ionosphere. *Journal of Geophysical Research*, *92*, 12,255–12,266. https://doi.org/10.1029/JA092iA11p12255

Baumjohann, W., & Kamide, Y. (1984). Hemispherical Joule heating and the AE indices. *Journal of Geophysical Research*, *89*(A1), 383–388. https://doi.org/10.1029/JA089iA01p00383

Chappell, C. R., Moore, T. E., & Waite, J. H. J. (1987). The ionosphere as a fully adequate source of plasma for the Earth's magnetosphere. *Journal of Geophysical Research*, *92*,A6 5896–5910. https://doi.org/10.1029/JA092iA06p05896

Chun, F. K., Knipp, D. J., McHarg, M. G., Lacey, J. R., Lu, G., & Emery, B. A. (2002). Joule heating patterns as a function of polar cap index. *Journal of Geophysical Research*, *107*(A7), 1119. https://doi.org/10.1029/2001JA000246

Cnossen, I., & Richmond, A. D. (2012). How changes in the tilt angle of the geomagnetic dipole affect the coupled magnetosphere-ionosphere-thermosphere system. *Journal of Geophysical Research*, *117*, A10317. https://doi.org/10.1029/2012JA018056

Engwall, E., Eriksson, A. I., Cully, C. M., André, M., Torbert, R., & Vaith, H. (2009). Earth's ionospheric outflow dominated by hidden cold plasma. *Nature Geoscience*, *2*, 24–27. https://doi.org/10.1038/ngeo387

Fairfield, D. H., & Scudder, J. D. (1985). Polar rain: Solar coronal electrons in the Earth's magnetosphere. *Journal of Geophysical Research*, *90*(A5), 4055–4068. https://doi.org/10.1029/JA090iA05p04055

Förster, M., & Cnossen, I. (2013). Upper atmosphere differences between northern and southern high latitudes: The role of magnetic field asymmetry. *Journal of Geophysical Research: Space Physics*, *118*, 5951–5966. https://doi.org/10.1002/jgra.50554

Ganguli, S. B. (1996). The polar wind. *Reviews of Geophysics*, *34*, 311–348. https://doi.org/10.1029/96RG00497
Glocer, A., Kitamura, N., Toth, G., & Gombosi, T. (2012). Modeling solar zenith angle effects on the polar wind. *Journal of Geophysical Research*, *117*, A04318. https://doi.org/10.1029/2011JA017136
Goodrich, C. C., & Scudder, J. D. (1984). The adiabatic energy change of plasma electrons and the frame dependence of the cross-shock potential at collisionless magnetosonic shock waves. *Journal of Geophysical Research*, *89*(A8), 6654–6662. https://doi.org/10.1029/JA089iA08p06654
Gosling, J. T., Baker, D. N., Bame, S. J., Feldman, W. C., Zwickl, R. D., & Smith, E. J. (1985). North-south and dawn-dusk plasma asymmetries in the distant magnetotail lobes: ISEE 3. *Journal of Geophysical Research*, *90*(A7), 6354–6360. https://doi.org/10.1029/JA090iA07p06354
Green, A. E. S., & Stolarski, R. S. (1976). Analytic models of electron impact excitation cross sections. *Journal of Atmospheric and Terrestrial Physics*, *34*(10), 1703–1717. https://doi.org/10.1016/0021-9169(72)90030-X
Gussenhoven, M. S., & Madden, D. (1990). Monitoring the polar rain over a solar cycle: A polar rain index. *Journal of Geophysical Research*, *95*(A7), 10,399–10,416. https://doi.org/10.1029/JA095iA07p10399
Haaland, S., Lybekk, B., Maes, L., Laundal, K., Pedersen, A., Tenfjord, P., et al. (2017). North-south asymmetries in cold plasma density in the magnetotail lobes: Cluster observations. *Journal of Geophysical Research: Space Physics*, *122*, 136–149. https://doi.org/10.1002/2016JA023404
Kitamura, N., Ogawa, Y., Nishimura, Y., Terada, N., Ono, T., Shinbori, A., et al. (2011). Solar zenith angle dependence of plasma density and temperature in the polar cap ionosphere and low-altitude magnetosphere during geomagnetically quiet periods at solar maximum. *Journal of Geophysical Research*, *116*, A08227. https://doi.org/10.1029/2011JA016631
Laundal, K. M., Cnossen, I., Milan, S. E., Haaland, S. E., Coxon, J., Pedatella, N. M., et al. (2017). North-south asymmetries in Earth's magnetic field: Effects on high-latitude geospace. *Space Science Review*, *206*(14), 225–257. https://doi.org/10.1007/s11214-016-0273-0
Li, K., Wei, Y., André, M., Eriksson, A., Haaland, S., Kronberg, E. A., et al. (2017). Cold ion outflow modulated by the solar wind energy input and tilt of the geomagnetic dipole. *Journal of Geophysical Research: Space Physics*, *122*, 10,658–10,668. https://doi.org/10.1002/2017JA024642
Li, K., Wei, Y., Haaland, S., Kronberg, E. A., Rong, Z. J., Maes, L., et al. (2018). Estimating the kinetic energy budget of the polar wind outflow. *Journal of Geophysical Research: Space Physics*, *123*, 7917–7929. https://doi.org/10.1029/2018JA025819
Lu, G., Richmond, A. D., Lühr, H., & Paxton, L. (2016). High-latitude energy input and its impact on the thermosphere. *Journal of Geophysical Research: Space Physics*, *121*, 7108–7124. https://doi.org/10.1002/2015JA022294
Lybekk, B., Pedersen, A., Haaland, S., Svenes, K., Fazakerley, A. N., Masson, A., et al. (2012). Solar cycle variations of the Cluster spacecraft potential and its use for electron density estimations. *Journal of Geophysical Research*, *117*, A01217. https://doi.org/10.1029/2011JA016969
Maes, L., Maggiolo, R., de Keyser, J., André, M., Eriksson, A. I., Haaland, S., et al. (2017). Solar illumination control of the polar wind. *Journal of Geophysical Research: Space Physics*, *122*, 11,468–11,480. https://doi.org/10.1002/2017JA024615
Moore, T. E., & Horwitz, J. L. (2007). Stellar ablation of planetary atmospheres. *Reviews of Geophysics*, *45*, RG3002. https://doi.org/10.1029/2005RG000194
Newell, P. T., Liou, K., & Wilson, G. R. (2009). Polar cap particle precipitation and aurora: Review and commentary. *Journal of Atmospheric and Solar-Terrestrial Physics*, *71*, 199–215. https://doi.org/10.1016/j.jastp.2008.11.004
Østgaard, N., Vondrak, R. R., Gjerloev, J. W., & Germany, G. (2002). A relation between the energy deposition by electron precipitation and geomagnetic indices during substorms. *Journal of Geophysical Research*, *107*(A9), 1246. https://doi.org/10.1029/2001JA002003
Picone, J. M., Hedin, A. E., Drob, D. P., & Aikin, A. C. (2002). NRLMSISE-00 empirical model of the atmosphere: Statistical comparisons and scientific issues. *Journal of Geophysical Research*, *107*(A12), 1468. https://doi.org/10.1029/2002JA009430
Prasad, S. S., Strickland, D. J., & Chiu, Y. T. (1985). Precipitating electron interaction with the atmosphere 2. The dayside cusp region. *Journal of Geophysical Research*, *90*(A11), 11,025–11,034. https://doi.org/10.1029/JA090iA11p11025
Richards, P. G., & Torr, D. G. (1985). Seasonal, diurnal and solar cycle variations of the limiting H+ flux in the Earth's topside ionosphere. *Journal of Geophysical Research*, *90*, 5261–5268. https://doi.org/10.1029/JA090iA06p05261
Riehl, K. B., & Hardy, D. A. (1986). Average characteristics of the polar rain and their relationship to the solar wind and the interplanetary magnetic field. *Journal of Geophysical Research*, *91*(A2), 1557–1571. https://doi.org/10.1029/JA091iA02p01557
Slavin, J. A., Smith, E. J., Sibeck, D. G., Baker, D. N., Zwickl, R. D., & Akasofu, S.-I. (1985). An ISEE 3 study of average and substorm conditions in the distant magnetotail. *Journal of Geophysical Research*, *90*,A11 10,875–10,895. https://doi.org/10.1029/JA090iA11p10875
Slinker, S. P., Taylor, R. D., & Ali, A. W. (1988). Electron energy deposition in atomic oxygen. *Journal of Applied Physics*, *63*. https://doi.org/10.1063/1.340491
Su, Y.-J., Horwitz, J. L., Wilson, G. R., Richards, P. G., Brown, D. G., & Ho, C. W. (1998). Self-consistent simulation of the photoelectron-driven polar wind from 120 km to 9 RE altitude. *Journal of Geophysical Research*, *103*,A2 2279–2296. https://doi.org/10.1029/97JA03085
Tsyganenko, N. A. (2002a). A model of the near magnetosphere with a dawn-dusk asymmetry 1. Mathematical structure. *Journal of Geophysical Research*, *107*(A8), 1179. https://doi.org/10.1029/2001A000219
Tsyganenko, N. A. (2002b). A model of the near magnetosphere with a dawn-dusk asymmetry 2. Parameterization and fitting to observations. *Journal of Geophysical Research*, *107*(A8), 1176. https://doi.org/10.1029/2001A000220
Varney, R. H., Solomon, S. C., & Nicolls, M. J. (2014). Heating of the sunlit polar cap ionosphere by reflected photoelectrons. *Journal of Geophysical Research Space Physics*, *119*, 8660–8684. https://doi.org/10.1002/2013JA019378
Wei, Y., Pu, Z., Zong, Q., Wan, W., Ren, Z., Fraenz, M., et al. (2014). Oxygen escape from the Earth during geomagnetic reversals: Implications to mass extinction. *Earth and Planetary Science Letters*, *394*, 94–98. https://doi.org/10.1016/j.epsl.2014.03.018
Yamauchi, M. (2019). Terrestrial ion escape and relevant circulation in space. *Annales Geophysicae*. https://doi.org/10.5194/angeo-37-1197-2019
Yau, A. W., Takumi, A., & Peterson, W. K. (2007). The polar wind: Recent observations. *Journal of Atmospheric and Solar-Terrestrial Physics*, *69*(16), 1936–1983. https://doi.org/10.1016/j.jastp.2007.08.010